Single-photon frequency conversion by exploiting quantum interference

Matthew Bradford and Jung-Tsung Shen*

Department of Electrical and Systems Engineering, Washington University in St. Louis, St. Louis, Missouri 63130, USA

(Received 4 February 2012; published 9 April 2012)

We present a scheme to achieve efficient single-photon frequency conversion by exploiting quantum interference between different transition pathways for single-photon states. As an example, we discuss the single-photon frequency-conversion process in the configuration wherein a Λ-type (Lambda-type) three-level quantum emitter is coupled to a Sagnac interferometer. It is shown that the efficiency of the frequency conversion approaches unity in the ideal case. A real-space theoretical approach and a pseudospectral numerical method are developed, which facilitate the computation for the full spatiotemporal dynamics of the scattering process.

DOI: 10.1103/PhysRevA.85.043814 PACS number(s): 42.50.Ct, 42.65.−k

I. INTRODUCTION

The capability to dynamically shift the frequency of light at the single-photon level is critical for many applications in quantum information processing. For example, by modulating the frequency of single photons through discrete frequency changes, the quantum analog of frequency-shift keying in optical communication [1] could be realized. Efficient optical frequency conversion of light has been explored in the large-photon-flux limit [2,3]. In this paper, we explore the possibility of achieving frequency conversion of light in the quantum regime of single photons and seek an architecture that is readily amenable to solid-state implementations. The requisite optical nonlinearities to achieve frequency conversion, although generally very weak at ultralow light levels [4], could still be exploited and tailored through proper design. Several schemes for producing single-photon nonlinearities have been proposed, such as a single-photon transistor, where the presence of a single gate photon is sufficient to control the propagation of subsequent signal photons [5]. Another example is a deterministic photonic entangler, wherein two photons can exchange energy and exhibit resonance fluorescence, analogous to a $\chi^{(3)}$ process [6]. These few-photon nonlinear devices rely on the existence of strong photon-photon interactions, imposing stringent operating conditions for photons and the emitter, such as impedance matching and pulse split [5], as well as constraints on relative photon arrival times set by the spontaneous emission lifetime of the quantum emitter. Consequently, it would be advantageous if some of the nonlinear optical processes could be accomplished using only one photon; these single-photon devices are anticipated to be more robust than those requiring few photons for the same nonlinear processes (e.g., the quantum state transfer of single photons). In this paper we exploit quantum interference between single-photon transition pathways to achieve efficient single-photon frequency conversion. We show that the efficiency approaches unity in the ideal case. Moreover, we numerically demonstrate this capability by simulating the single-photon frequency-conversion process using the D^0-DX^0 transition in a GaAs quantum dot with experimentally measured physical parameters. It is shown that the conversion efficiency can be larger than 80% even in the presence of dissipation, allowing practical applications. Before we describe in detail the theoretical formulation, we begin with a physical picture of the frequency-conversion process [7]. The basis of the system is a Λ-type three-level quantum emitter with energy levels shown in Fig. 1(a) coupled to a one-dimensional waveguide. When the emitter initially in the $|1\rangle$ state is excited by an incoming photon, it can spontaneously decay to either of the low-lying states $|1\rangle$ or $|2\rangle$ and emit a photon. If the emitter decays to state $|2\rangle$, the outgoing photon will be frequency downshifted [Fig. 1(a), top]. Note that frequency up conversion can also be achieved if the emitter is initialized to state $|2\rangle$ and decays to state $|1\rangle$ [Fig. 1(a), bottom].

Consider the following typical scattering process: if an incoming photon encounters the emitter directly [Fig. 1(b)], the outgoing photon will be in a spectral superposition of frequency-shifted and -unshifted waves (as well as a spatial superposition of reflected and transmitted waves), with a maximum frequency-shift probability of one half (considering both the reflected and transmitted waves). The conversion efficiency can be significantly enhanced by exploiting quantum interference: if the input photon is in a spatial superposition of incoming from the left and incoming from the right, emission from the $|1\rangle \leftrightarrow |3\rangle$ transition (in the down-conversion case) or the $|2\rangle \leftrightarrow |3\rangle$ (in the up-conversion case) can be completely suppressed through quantum interference. That is, the emitter undergoes a complete population state transfer, induced by the input photon. One realization of the desired quantum interference is achieved by coupling the emitter to a Sagnac interferometer [8,9] [Fig. 1(c)]. When a photon incoming to port a encounters the 50 : 50 coupler, it is split into counterpropagating clockwise (cw) and counterclockwise (ccw) modes which interfere constructively at the emitter and suppress emission from the $|1\rangle \leftrightarrow |3\rangle$ transition. The frequency-shift probability reaches its maximum when the coupling strengths Γ_1 and Γ_2 are equal. Moreover, the Sagnac interferometer geometry provides the ability to dynamically control the frequency-shift process by using a tunable phase shifter as shown in Fig. 1(c) to introduce a relative phase θ between the cw and ccw modes. For a relative phase $\theta = \pi$ between the cw and ccw modes, the photon will not interact with the emitter at all, and the frequency of the photon will

*jushen@ese.wustl.edu

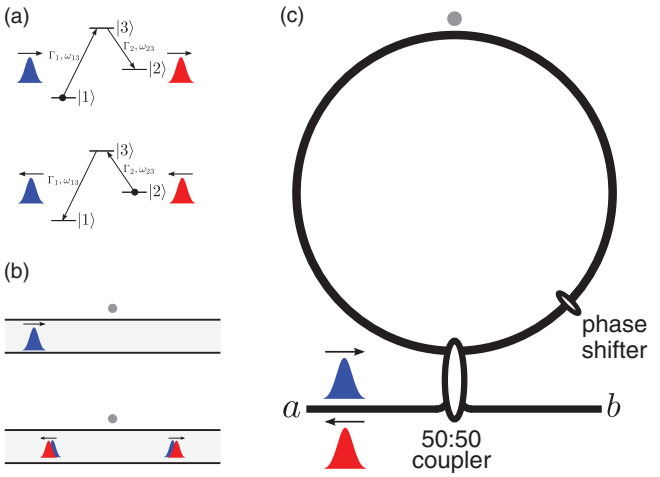

FIG. 1. (Color online) Emitter energy levels and system schematic. (a) Schematic Λ-type three-level quantum emitter with transition frequencies ω_{13} and ω_{23}. Γ_1 and Γ_2 are the coupling strengths of each transition to the waveguide. The top diagram corresponds to frequency down conversion and the bottom diagram corresponds to up conversion. (b) Emitter (gray) coupled to a one-dimensional waveguide. The top part shows a photonic pulse incoming from the left. The bottom part shows the state after scattering, with the outgoing photon in a spectral superposition of frequency shifted and unshifted and a spatial superposition of reflected and transmitted. (c) Emitter coupled to a Sagnac interferometer.

be unshifted. The quantum interference effects have been previously explored in the context of single-photon switching [10].

The paper is organized as follows: In Sec. II, we present the theory of a single-photon scattering process in which frequency conversion occurs through interaction with a Λ-type three-level quantum emitter. Using a real-space Hamiltonian, the governing equations of motion are derived to obtain the full spatiotemporal dynamics of the scattering process. We also investigate the steady-state frequency-conversion process to derive transport properties which give deeper insight into the single-photon frequency-conversion process. We then detail a scattering matrix description, which is the most compact description of the scattering process. In Sec. III, we apply the theoretical framework to determine the output when the input is a photonic pulse with finite bandwidth. We then discuss the conversion efficiency for finite-bandwidth scattering and present results for several practically important pulse types. We further discuss effects due to emitter dissipation and relative pulse delay. Finally, in Sec. IV, we compare and contrast our proposal with other schemes and discuss the experimental feasibility of our scheme, as well as the current state of the art in single-photon frequency-conversion experiments. In the appendix, we describe an efficient numerical scheme combining pseudospectral methods with nonuniform gridding to computationally evaluate the system dynamics.

II. HAMILTONIAN, EQUATIONS OF MOTION, AND SCATTERING MATRIX

Here we detail a complete theoretical framework for the frequency-conversion process. We begin by presenting the Hamiltonian of the system and deriving the governing equations of motion. The system consists of a Λ-type three-level quantum emitter coupled to a Sagnac interferometer, and is described by a Dicke-type Hamiltonian in real space [11]. The Hamiltonian H is given by

$$H = H_{\mathrm{p}} + H_{\mathrm{q}} + H_{\mathrm{i}}, \tag{1}$$

where H_{p} is the free photonic Hamiltonian, H_{q} is the free quantum emitter Hamiltonian, and H_{i} describes the interaction between the photon and emitter. H_{p} is given by

$$H_{\mathrm{p}} = \int dx \hbar \{c_{\mathrm{R}}^{\dagger}(x)(-iv_{\mathrm{g}}\partial_x)c_{\mathrm{R}}(x) + c_{\mathrm{L}}^{\dagger}(x)(iv_{\mathrm{g}}\partial_x)c_{\mathrm{L}}(x)\}, \tag{2}$$

where $c_{\mathrm{R}}^{\dagger}(x)$ and $c_{\mathrm{R}}(x)$ are creation and annihilation operators, respectively, for a right-moving photon at position x, and $c_{\mathrm{L}}^{\dagger}(x)$ and $c_{\mathrm{L}}(x)$ are creation and annihilation operators, respectively, for a left-moving photon at position x. Note that, inside the Sagnac interferometer loop, right-moving corresponds to clockwise (cw) and left-moving corresponds to counterclockwise (ccw); v_{g} is the group velocity of the photon. The Hamiltonian of the quantum emitter H_{q} is

$$H_{\mathrm{q}} = \hbar(\omega_1 a_1^{\dagger}a_1 + \omega_2 a_2^{\dagger}a_2 + \omega_3 a_3^{\dagger}a_3), \tag{3}$$

where $a_i^{\dagger}$ and a_i are creation and annihilation operators, respectively, and $a_i^{\dagger}a_i = \hat{n}_i$ is the number operator for the emitter $|i\rangle$ state. The interaction term describes the scattering between photons and the emitter and is given by

$$H_{\mathrm{i}} = \int dx \hbar\delta(x)(V_1\{[c_{\mathrm{R}}^{\dagger}(x) + c_{\mathrm{L}}^{\dagger}]\sigma_{13} + [c_{\mathrm{R}}(x) + c_{\mathrm{L}}]\sigma_{31}\} + V_2\{[c_{\mathrm{R}}^{\dagger}(x) + c_{\mathrm{L}}^{\dagger}(x)]\sigma_{23} + [c_{\mathrm{R}}(x) + c_{\mathrm{L}}(x)]\sigma_{32}\}), \tag{4}$$

where $\sigma_{ij} = a_i^{\dagger}a_j$ is the transition operator from emitter state $|j\rangle$ to emitter state $|i\rangle$; V_1 and V_2 describe the interaction between each transition dipole moment and the photonic field; the emitter is located at $x = 0$ [for an emitter at $x = x_{\mathrm{q}}$, $\delta(x)$ must be replaced by $\delta(x - x_{\mathrm{q}})$]. H_{i} describes all absorption and emission processes of photons by the quantum emitter. For example, the term proportional to σ_{13} describes a quantum emitter transition from the excited $|3\rangle$ state to the $|1\rangle$ ground state and the spontaneous emission of either a left- or right-moving photon. The state $|\psi(t)\rangle$ describing the system is determined by the Schrödinger equation $i\hbar\partial_t|\psi\rangle = H|\psi\rangle$ for any given initial state $|\psi(t_0)\rangle$ at time t_0. We note that the dipole-field coupling strengths V_1 and V_2 depend on the vector nature of the dipole moment of each transition. A detailed *a priori* estimate is rather involved. For a given configuration, V_1 and V_2 can be estimated from the radiative spontaneous emission rates as described in Sec. II C.

A. Time-dependent description

Here we describe the time-dependent description of the scattering problem, which allows the computation of the full spatiotemporal dynamics. When the input consists of only one

photon, the general state is

$$|\psi\rangle = \int dx \{\phi_{1R}(x,t)c_R^\dagger(x)e^{-i\omega_1 t}a_1^\dagger + \phi_{1L}(x,t)c_L^\dagger(x)e^{-i\omega_1 t}a_1^\dagger + \phi_{2R}(x,t)c_R^\dagger(x)e^{-i\omega_2 t}a_2^\dagger + \phi_{2L}(x,t)c_L^\dagger(x)e^{-i\omega_2 t}a_2^\dagger\}|0\rangle + e_3(t)e^{-i\omega_3 t}a_3^\dagger|0\rangle, \tag{5}$$

where $\phi_{1R}(x,t)$, $\phi_{1L}(x,t)$, $\phi_{2R}(x,t)$, and $\phi_{2L}(x,t)$ are the amplitudes for right- or left-moving photons when the emitter is in state $|1\rangle$ or $|2\rangle$ and e_3 is the excitation amplitude of the quantum emitter in the $|3\rangle$ state. In Eq. (5), the time dependence of each emitter state is explicitly separated for convenience, such that the time dependence for the photonic part remains apparent throughout the computation. Solving the Schrödinger equation $i\hbar\partial_t|\psi\rangle = H|\psi\rangle$ yields the governing equations of motion

$$\begin{aligned}
i\partial_t\phi_{1R}(x,t)e^{-i\omega_1 t} &= -iv_g\partial_x\phi_{1R}(x,t)e^{-i\omega_1 t} + \omega_1\phi_{1R}(x,t)e^{-i\omega_1 t} + V_1\delta(x)e_3(t)e^{-i\omega_3 t},\\
i\partial_t\phi_{1L}(x,t)e^{-i\omega_1 t} &= +iv_g\partial_x\phi_{1L}(x,t)e^{-i\omega_1 t} + \omega_1\phi_{1L}(x,t)e^{-i\omega_1 t} + V_1\delta(x)e_3(t)e^{-i\omega_3 t},\\
i\partial_t\phi_{2R}(x,t)e^{-i\omega_2 t} &= -iv_g\partial_x\phi_{2R}(x,t)e^{-i\omega_2 t} + \omega_2\phi_{2R}(x,t)e^{-i\omega_2 t} + V_2\delta(x)e_3(t)e^{-i\omega_3 t},\\
i\partial_t\phi_{2L}(x,t)e^{-i\omega_2 t} &= +iv_g\partial_x\phi_{2L}(x,t)e^{-i\omega_2 t} + \omega_2\phi_{2L}(x,t)e^{-i\omega_2 t} + V_2\delta(x)e_3(t)e^{-i\omega_3 t},\\
i\partial_t e_3(t)e^{-i\omega_3 t} &= \omega_3 e_3(t)e^{-i\omega_3 t} + V_1e^{-i\omega_1 t}\{\phi_{1R}(0,t)+\phi_{1L}(0,t)\} + V_2e^{-i\omega_2 t}\{\phi_{2R}(0,t)+\phi_{2L}(0,t)\}.
\end{aligned} \tag{6}$$

For any initial state, the full spatiotemporal dynamics of the system can be obtained by numerically solving the set of equations [Eqs. (6)]. The initial state is specified by $\phi_{1R}(x,0)$, $\phi_{1L}(x,0)$, $\phi_{2R}(x,0)$, $\phi_{2L}(x,0)$, and $e_3(0)$.

B. Time-dependent description (one-mode chiral model)

Equations (6) fully describe the dynamics of the system and are applicable in either direct incidence [Fig. 1(b)] or in the Sagnac interferometer geometry [Fig. 1(c)]. However, due to the inherent symmetry in a Sagnac interferometer, it is convenient to cast the description in terms of even and odd modes, defined by the following operators:

$$\begin{aligned}
c_e^\dagger(x) &= \frac{1}{\sqrt{2}}[c_R^\dagger(x) + c_L^\dagger(-x)],\\
c_e(x) &= \frac{1}{\sqrt{2}}[c_R(x) + c_L(-x)],\\
c_o^\dagger(x) &= \frac{1}{\sqrt{2}}[c_R^\dagger(x) - c_L^\dagger(-x)],\\
c_o(x) &= \frac{1}{\sqrt{2}}[c_R(x) - c_L(-x)],
\end{aligned} \tag{7}$$

where $c_e^\dagger(x)$ and $c_e(x)$ are the even creation and annihilation operators, respectively, and $c_o^\dagger(x)$ and $c_o(x)$ are the odd creation and annihilation operators, respectively. Using the even and odd operators, H_p becomes

$$H_p = \hbar\int dx\{c_e^\dagger(x)(-iv_g\partial_x)c_e(x) + c_o^\dagger(x)(-iv_g\partial_x)c_o(x)\}. \tag{8}$$

The interaction Hamiltonian becomes

$$H_i = \int dx\hbar\delta(x)\{\sqrt{2}V_1[c_e^\dagger(x)\sigma_{13} + c_e(x)\sigma_{31}] + \sqrt{2}V_2[c_e^\dagger(x)\sigma_{23} + c_e(x)\sigma_{32}]\}, \tag{9}$$

which contains only even mode operators $c_e^\dagger(x)$ and $c_e(x)$, reflecting the symmetry of the system. Thus, even modes are scattered into even modes and odd modes experience no scattering. The general state of the system [Eq. (5)] is transformed accordingly:

$$|\psi\rangle = \sum_{i=1,2}\int dx\{\phi_{ie}(x,t)c_e^\dagger(x) + \phi_{io}(x,t)c_o^\dagger(x)\} \times e^{-i\omega_i t}a_i^\dagger|0\rangle + e_3(t)e^{-i\omega_3 t}a_3^\dagger|0\rangle, \tag{10}$$

where $\phi_{ie}(x,t) \equiv \frac{1}{\sqrt{2}}[\phi_{iR}(x,t) + \phi_{iL}(-x,t)]$ and $\phi_{io}(x,t) \equiv \frac{1}{\sqrt{2}}[\phi_{iR}(x,t) - \phi_{iL}(-x,t)]$ are the wave functions of the photon in even and odd states, respectively. When expressed in terms of even and odd fields, the equations of motion [Eqs. (6)] become

$$\begin{aligned}
i\partial_t\phi_{1e}(x,t)e^{-i\omega_1 t} &= -iv_g\partial_x\phi_{1e}(x,t)e^{-i\omega_1 t} + \omega_1\phi_{1e}(x,t)e^{-i\omega_1 t} + \sqrt{2}V_1\delta(x)e_3(t)e^{-i\omega_3 t},\\
i\partial_t\phi_{2e}(x,t)e^{-i\omega_2 t} &= -iv_g\partial_x\phi_{2e}(x,t)e^{-i\omega_2 t} + \omega_2\phi_{2e}(x,t)e^{-i\omega_2 t} + \sqrt{2}V_2\delta(x)e_3(t)e^{-i\omega_3 t},\\
i\partial_t\phi_{1o}(x,t)e^{-i\omega_1 t} &= -iv_g\partial_x\phi_{1o}(x,t)e^{-i\omega_1 t} + \omega_1\phi_{1o}(x,t)e^{-i\omega_1 t},\\
i\partial_t\phi_{2o}(x,t)e^{-i\omega_2 t} &= -iv_g\partial_x\phi_{2o}(x,t)e^{-i\omega_2 t} + \omega_2\phi_{2o}(x,t)e^{-i\omega_2 t},\\
i\partial_t e_3(t)e^{-i\omega_3 t} &= \omega_3 e_3(t)e^{-i\omega_3 t} + \sqrt{2}V_1\phi_{1e}(0,t)e^{-i\omega_1 t} + \sqrt{2}V_2\phi_{2e}(0,t)e^{-i\omega_2 t}.
\end{aligned} \tag{11}$$

When ϕ_{1o} and ϕ_{2o} are zero initially, they remain zero for any later time. The system is therefore described completely by the even modes. In this paper, we call this the one-mode chiral model.

C. Steady state solutions

The set of equations [Eqs. (6)] describes the full spatiotemporal dynamics of the system. Here we focus on the steady state solutions (i.e., eigenstates of the system) to derive the transmission amplitudes and gain deeper insights. In steady state, the entire system oscillates at a single frequency ω_t. For an initial state in which the incoming photon is monochromatic with frequency ω and the emitter is in the ground state with energy $\hbar\omega_1$, the total energy is $\hbar\omega_t = \hbar(\omega_1 + \omega)$. ω_t is conserved throughout the scattering process, which allows us to determine the time dependence of each component. We first develop the transmission properties for the direct incidence case [Fig. 1(b)] and show that the total frequency-shift probability is at most one half. Since, for an energy eigenstate, every term in Eq. (5) must have the same time dependence, it follows that

$$\begin{aligned}
\phi_{1R}(x,t) &= \phi_{1R}(x)e^{-i\omega t},\\
\phi_{1L}(x,t) &= \phi_{1L}(x)e^{-i\omega t},\\
\phi_{2R}(x,t) &= \phi_{2R}(x)e^{-i(\omega-\omega_{12})t},\\
\phi_{2L}(x,t) &= \phi_{2L}(x)e^{-i(\omega-\omega_{12})t},\\
e_3(t) &= e_3(\omega)e^{-i(\omega-\omega_{13})t},
\end{aligned} \tag{12}$$

where $\phi_{1R}(x)$, $\phi_{1L}(x)$, $\phi_{2R}(x)$, and $\phi_{2L}(x)$ give the spatial dependence of the photonic amplitudes and $e_3(\omega)$ is the excitation amplitude in steady state. We then make the following ansatz on the spatial dependence of the photonic amplitudes (which is numerically confirmed as described in the appendix):

$$\begin{aligned}
\phi_{1R}(x) &= e^{ik_1x}[\theta(-x) + t_1\theta(x)],\\
\phi_{1L}(x) &= e^{-ik_1x}r_1\theta(-x),\\
\phi_{2R}(x) &= e^{ik_2x}t_2\theta(x),\\
\phi_{2L}(x) &= e^{-ik_2x}r_2\theta(-x),
\end{aligned} \tag{13}$$

where $k_1 = \omega/v_g$ and $k_2 = (\omega - \omega_{12})/v_g$. $|t_1|^2$ and $|t_2|^2$ give the probability that a photon of single frequency ω will be transmitted and and leave the emitter in state $|1\rangle$ (thereby experiencing no frequency shift) or in state $|2\rangle$ (thereby experiencing a frequency shift), respectively. $|r_1|^2$ and $|r_2|^2$ give the probability that a photon of single frequency ω will be reflected and and leave the emitter in state $|1\rangle$ (thereby experiencing no frequency shift) or in state $|2\rangle$ (thereby experiencing a frequency shift of ω_{12}), respectively. After substituting the amplitudes given by Eqs. (12) and (13) into the equations of motion [Eqs. (6)], the equations of motion reduce to

$$\begin{aligned}
-iv_g(t_1 - 1) + e_3V_1 &= 0,\\
-iv_gr_1 + e_3V_1 &= 0,\\
-iv_gt_2 + e_3V_2 &= 0,\\
-iv_gr_2 + e_3V_2 &= 0,\\
\tfrac{1}{2}V_1(t_1 + r_1 + 1) + \tfrac{1}{2}V_2(t_2 + r_2) &= (\omega - \omega_{13})e_3.
\end{aligned} \tag{14}$$

From Eqs. (14), we obtain the transmission, reflection, and excitation amplitudes:

$$t_1(\omega) = \frac{(\omega - \omega_{13}) + i\Gamma_2}{(\omega - \omega_{13}) + i(\Gamma_1 + \Gamma_2)}, \tag{15}$$

$$r_1(\omega) = -\frac{i\Gamma_1}{(\omega - \omega_{13}) + i(\Gamma_1 + \Gamma_2)}, \tag{16}$$

$$t_2(\omega) = -\frac{i\sqrt{\Gamma_1\Gamma_2}}{(\omega - \omega_{13}) + i(\Gamma_1 + \Gamma_2)}, \tag{17}$$

$$r_2(\omega) = -\frac{i\sqrt{\Gamma_1\Gamma_2}}{(\omega - \omega_{13}) + i(\Gamma_1 + \Gamma_2)}, \tag{18}$$

$$e_3(\omega) = \frac{V_1}{(\omega - \omega_{13}) + i(\Gamma_1 + \Gamma_2)}, \tag{19}$$

where $\Gamma_1 = V_1^2/v_g$ and $\Gamma_2 = V_2^2/v_g$ are the radiative spontaneous decay rates for each transition and give the linewidth of all spectra. In Sec. III B, we show that the presence of dissipation will modify the linewidth. $|t_1|^2$ has an inverted Lorentzian line shape, while $|r_1|^2$, $|t_2|^2$, and $|r_2|^2$ have Lorentzian line shapes. All spectra have full width at half maximum (FWHM) $2\Gamma \equiv 2(\Gamma_1 + \Gamma_2)$. From these expressions, the transport of a photon on resonance with the $|1\rangle \leftrightarrow |3\rangle$ transition is solely determined by the dimensionless quantity $\alpha \equiv \Gamma_1/\Gamma_2$. In particular, $|t_1(\omega_{13})|^2 = 1/(1+\alpha)^2$, $|r_1(\omega_{13})|^2 = \alpha^2/(1+\alpha)^2$, $|t_2(\omega_{13})|^2 = \alpha/(1+\alpha)^2$, and $|r_2(\omega_{13})|^2 = \alpha/(1+\alpha)^2$. For large values of α (i.e., $\Gamma_1 \gg \Gamma_2$), $|t_2|^2$ and $|r_2|^2$ become small, and the transmission and reflection behavior reduces to the case of scattering by a two-level emitter [12]. The total frequency-shift probability is maximal for $\alpha = 1$, for which $|t_2(\omega_{13})|^2 = 1/4$ and $|r_2(\omega_{13})|^2 = 1/4$, so the combined on-resonance frequency-shift probability is $1/2$. The transmission, reflection, and excitation spectra are plotted in Fig. 2, where the excitation spectrum is normalized for convenience.

D. Steady state solutions (one-mode chiral model)

Here we derive the steady state transmission amplitudes in the Sagnac interferometer geometry. The eigenstate wave functions in Eq. (10) have the form

$$\begin{aligned}
\phi_{1e}(x,t) &= \phi_{1e}(x)e^{-i\omega t},\\
\phi_{2e}(x,t) &= \phi_{2e}(x)e^{-i(\omega-\omega_{12})t},\\
\phi_{1o}(x,t) &= \phi_{1o}(x)e^{-i\omega t},\\
\phi_{2o}(x,t) &= \phi_{2o}(x)e^{-i(\omega-\omega_{12})t},\\
e_3(t) &= e_3(\omega)e^{-i(\omega-\omega_{13})t},
\end{aligned} \tag{20}$$

where $\phi_{1e}(x)$, $\phi_{2e}(x)$, $\phi_{1o}(x)$, and $\phi_{2o}(x)$ give the spatial dependence of the photonic amplitudes and $e_3(\omega)$ is the excitation amplitude in steady state, $\omega_{13} = \omega_3 - \omega_1$ is the frequency of the $|1\rangle \leftrightarrow |3\rangle$ transition, and $\omega_{12} = \omega_2 - \omega_1$ is the frequency separation of the quantum emitter $|1\rangle$ and $|2\rangle$ states. In a Sagnac interferometer, when the cw and ccw modes are in phase ($\theta = 0$), $\phi_{1o}(x) = \phi_{2o}(x) = 0$ and only even modes will propagate in the Sagnac interferometer. We then make the following ansatz on the spatial dependence of the even photonic amplitudes (again, the validity of the ansatz is confirmed numerically as described in the appendix):

$$\begin{aligned}
\phi_{1e}(x) &= e^{ik_1x}[\theta(-x) + t_1\theta(x)],\\
\phi_{2e}(x) &= e^{ik_2x}t_2\theta(x),
\end{aligned} \tag{21}$$

where again $k_1 = \omega/v_g$, $k_2 = (\omega - \omega_{12})/v_g$, and t_1 and t_2 are transmission amplitudes. After substituting the amplitudes given by Eqs. (20) and (21) into the equations of motion

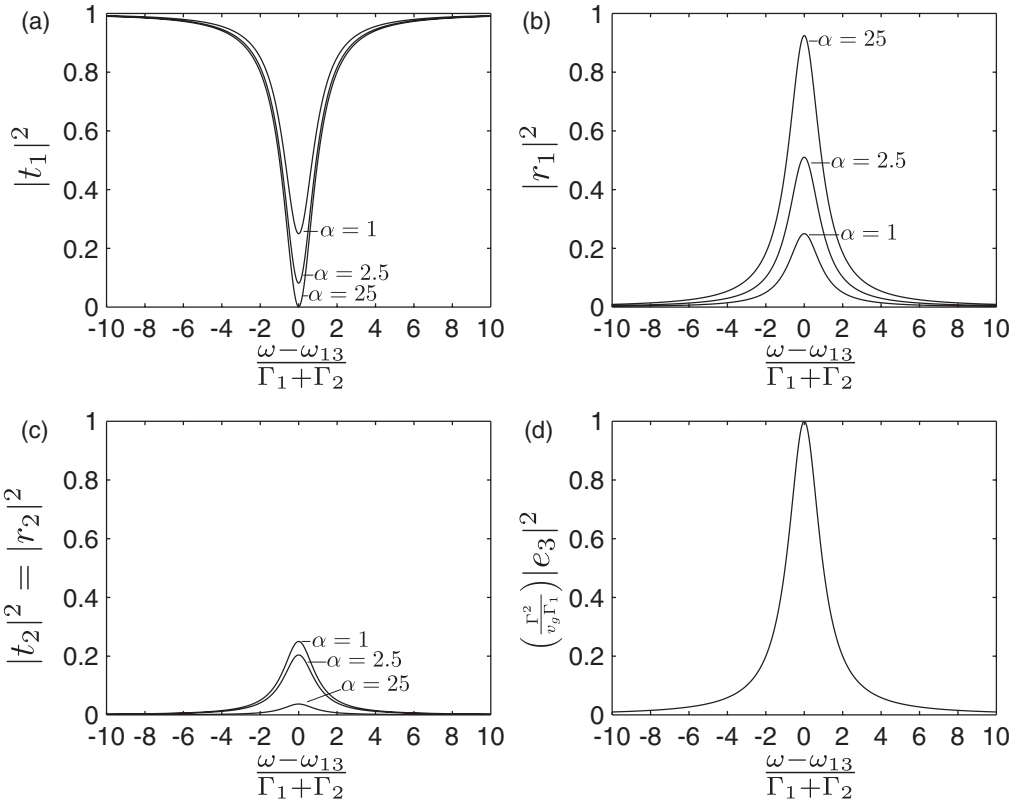

FIG. 2. Transmission, reflection, and emitter excitation for the case corresponding to Fig. 1(b). (a) Elastic transmission $|t_1|^2$. (b) Elastic reflection $|r_1|^2$. (c) Inelastic transmission $|t_2|^2$ and reflection $|r_2|^2$. (d) Normalized emitter excitation spectrum.

[Eqs. (11)], the equations of motion reduce to

$$\begin{aligned} -iv_g(t_1-1)+e_3\sqrt{2}V_1 &= 0,\\ -iv_g t_2+e_3\sqrt{2}V_2 &= 0,\\ \frac{1}{\sqrt{2}}V_1(t_1+1)+\frac{1}{\sqrt{2}}V_2 t_2 &= (\omega-\omega_{13})e_3. \end{aligned} \tag{22}$$

From Eqs. (22) we obtain the transmission and excitation amplitudes

$$\begin{aligned} t_1(\omega) &= \frac{(\omega-\omega_{13})-i(\Gamma_1-\Gamma_2)}{(\omega-\omega_{13})+i(\Gamma_1+\Gamma_2)},\\ t_2(\omega) &= -\frac{i2\sqrt{\Gamma_1\Gamma_2}}{(\omega-\omega_{13})+i(\Gamma_1+\Gamma_2)},\\ e_3(\omega) &= \frac{\sqrt{2}V_1}{(\omega-\omega_{13})+i(\Gamma_1+\Gamma_2)}, \end{aligned} \tag{23}$$

where again $\Gamma_1 = V_1^2/v_g$ and $\Gamma_2 = V_2^2/v_g$. $|t_1(\omega)|^2$ and $|t_2(\omega)|^2$ give the probability that an input photon at a single frequency ω will leave the emitter in state $|1\rangle$ (thereby experiencing no frequency shift) or state $|2\rangle$ (thereby experiencing a frequency downshift of ω_{12}), respectively, after scattering. The on-resonance transmission is again determined completely by the dimensionless parameter α. Specifically, $|t_1(\omega_{13})|^2 = (1-\alpha)^2/(1+\alpha)^2$ and $|t_2(\omega_{13})|^2 = 4\alpha/(1+\alpha)^2$, so when the incoming photon is on resonance ($\omega = \omega_{13}$) and the transition strengths are equal ($\Gamma_1 \sim \Gamma_2$), the frequency-shift probability approaches unity. The transmission spectra for the Sagnac interferometer geometry are plotted in Fig. 3 for several values of α. In Figs. 3(c) and 3(d), the transmission spectra for $\alpha = 1$ are also compared to results obtained numerically. The excellent agreement confirms the validity of the ansatz given in Eq. (21).

If a phase shifter is used to introduce a relative phase of $\theta = \pi$ between the cw and ccw modes, only odd states will propagate in the Sagnac interferometer. The photonic modes will thus not interact with the emitter at all, corresponding to $|t_1|^2 = 1$, $|t_2|^2 = 0$ for all frequencies.

E. Scattering matrix

In scattering problems, one is interested in the initial states and the output states, of which the relation is completely specified by a scattering matrix. Ultimately, the scattering matrix encodes all transport properties. Here we describe the scattering matrix for a Λ-type emitter coupled to a Sagnac interferometer. For a photon of frequency ω input to port a of the Sagnac interferometer, with the quantum emitter initially in state $|1\rangle \equiv a_1^\dagger|0\rangle$, the initial state is a direct product of the photonic and emitter states

$$|\psi\rangle_{\text{in}} = \begin{pmatrix} |\omega\rangle \\ 0 \end{pmatrix} \bigotimes |1\rangle. \tag{24}$$

The 50 : 50 coupler, with scattering matrix

$$S_c = \frac{1}{\sqrt{2}}\begin{pmatrix} 1 & 1 \\ 1 & -1 \end{pmatrix}, \tag{25}$$

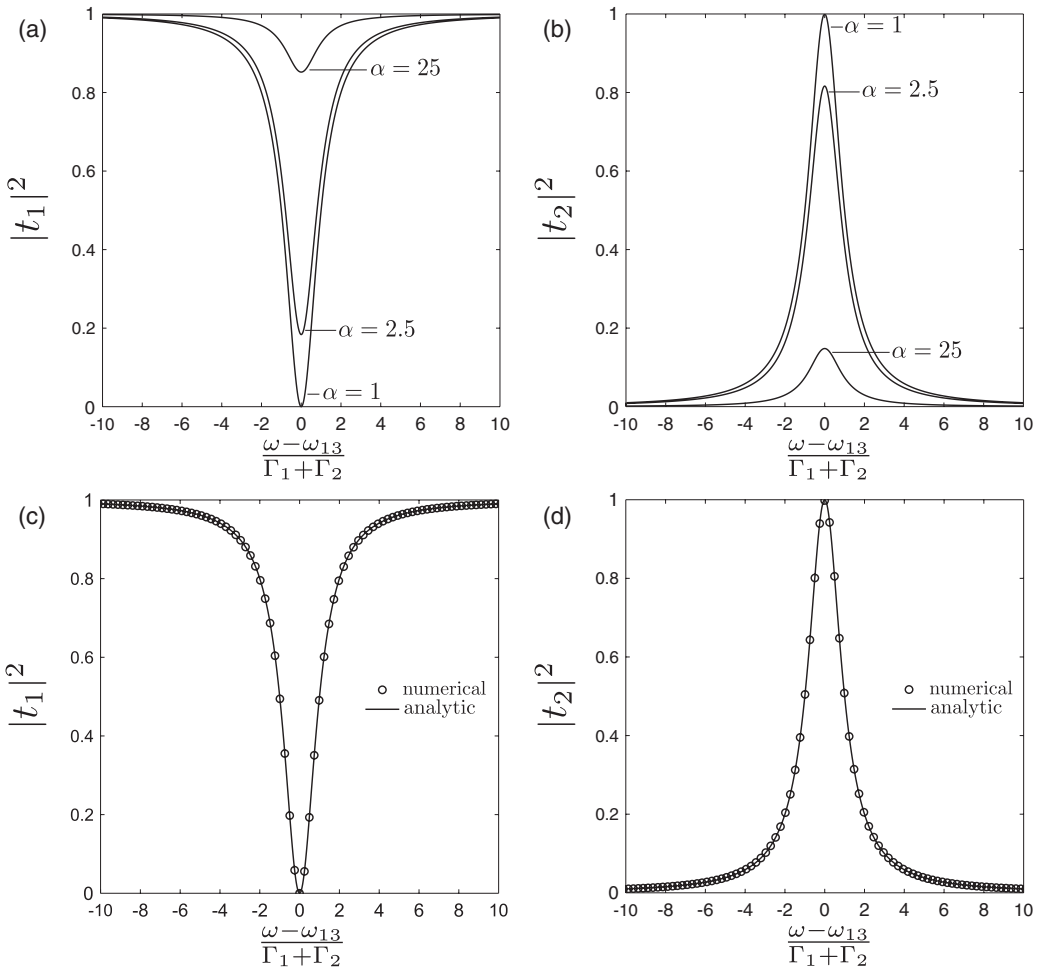

FIG. 3. Transmission spectra in Sagnac interferometer geometry. (a) Elastic transmission $|t_1|^2$. (b) Inelastic transmission $|t_2|^2$. (c) Comparison of $|t_1|^2$ with numerical results. (d) Comparison of $|t_2|^2$ with numerical results.

acts only on the photonic part of Eq. (24), yielding the state

$$|\psi\rangle = \frac{1}{\sqrt{2}}\begin{pmatrix}|\omega\rangle\\|\omega\rangle\end{pmatrix}\bigotimes|1\rangle. \tag{26}$$

The quantum emitter scattering matrix satisfies

$$S_q\left[\frac{1}{\sqrt{2}}\begin{pmatrix}|\omega\rangle\\|\omega\rangle\end{pmatrix}\bigotimes|1\rangle\right] \equiv \frac{1}{\sqrt{2}}\begin{pmatrix}t_1(\omega)|\omega\rangle\bigotimes|1\rangle + t_2(\omega)|\omega-\omega_{12}\rangle\bigotimes|2\rangle\\ t_1(\omega)|\omega\rangle\bigotimes|1\rangle + t_2(\omega)|\omega-\omega_{12}\rangle\bigotimes|2\rangle\end{pmatrix}. \tag{27}$$

Equations (26) and (27) correspond to even modes propagating in the loop. After propagation in the loop, which acts with scattering matrix

$$S_l = \begin{pmatrix}0 & 1\\ 1 & 0\end{pmatrix}, \tag{28}$$

and subsequent recombination in the coupler (again with scattering matrix S_c), the final output state is only in port a and is given by

$$|\psi\rangle_{\text{out}} = S_c S_l S_q S_c |\psi\rangle_{\text{in}}, = \begin{pmatrix}t_1(\omega)|\omega\rangle\bigotimes|1\rangle + t_2(\omega)|\omega-\omega_{12}\rangle\bigotimes|2\rangle\\ 0\end{pmatrix}. \tag{29}$$

The total scattering matrix S is then given by summing over the complete set of input and output states

$$S = \sum_{\omega}|\psi(\omega)\rangle_{\text{out in}}\langle\psi(\omega)|. \tag{30}$$

III. BEYOND SINGLE FREQUENCY: FINITE-BANDWIDTH SCATTERING

With the previous mathematical preparation, we now describe the output state when the input is a photonic pulse with finite bandwidth. Consider the situation in which a photon with amplitude $\phi_{\text{in}}(x,t)$ is injected through port a and the emitter is initially in the ground state $|1\rangle$. As previously described, only even modes propagate inside the loop (both before and after scattering). After traversing the 50 : 50 coupler but before scattering, the propagating mode is given by

$\phi_{1e,in}(x,t) = \frac{1}{\sqrt{2}}[\phi_{1cw,in}(x,t) + \phi_{1ccw,in}(-x,t)]$, where

$$\begin{aligned}\phi_{1cw,in}(x,t) &= \frac{1}{\sqrt{2}}\phi_{in}(x,t),\\ \phi_{1ccw,in}(x,t) &= \frac{1}{\sqrt{2}}\phi_{in}(-x,t),\end{aligned} \tag{31}$$

so one has $\phi_{1e,in}(x,t) = \phi_{in}(x,t)$; that is, the even state inside the loop before scattering $\phi_{1e,in}(x,t)$ has the same functional form as the input in port a. After scattering, the photonic states in the loop are described by the amplitudes $\phi_{1e,out}(x,t)$ and $\phi_{2e,out}(x,t)$, which are related to the input state by

$$\begin{aligned}\tilde{\phi}_{1e,out}(x,\omega) &= t_1(\omega)\tilde{\phi}_{1e,in}(x,\omega),\\ \tilde{\phi}_{2e,out}(x,\omega) &= t_2(\omega)\tilde{\phi}_{1e,in}(x,\omega),\end{aligned} \tag{32}$$

where $\tilde{\phi}(x,\omega) = \int dt\phi(x,t)e^{i\omega t}/\sqrt{2\pi}$ indicates the temporal Fourier transform. The state in the loop after scattering is

$$\begin{aligned}|\psi\rangle^{l}_{out} = &\frac{1}{\sqrt{2\pi}}\int d\omega e^{-i\omega t}\tilde{\phi}_{1e,out}(x,\omega)e^{-i\omega_1 t}c_e^{\dagger}(x)a_1^{\dagger}|0\rangle\\ &+\frac{1}{\sqrt{2\pi}}\int d\omega e^{-i\omega' t}\tilde{\phi}_{2e,out}(x,\omega)e^{-i\omega_2 t}c_e^{\dagger}(x)a_2^{\dagger}|0\rangle.\end{aligned} \tag{33}$$

ω' is uniquely determined by energy conservation, as described in Sec. II C. So, the scattered state inside the loop is

$$\begin{aligned}|\psi\rangle^{l}_{out} = &\frac{1}{\sqrt{2\pi}}\int d\omega e^{-i\omega t}\tilde{\phi}_{1e,out}(x,\omega)e^{-i\omega_1 t}c_e^{\dagger}(x)a_1^{\dagger}|0\rangle\\ &+\frac{1}{\sqrt{2\pi}}\int d\omega e^{-i(\omega-\omega_{12})t}\tilde{\phi}_{2e,out}(x,\omega)e^{-i\omega_2 t}c_e^{\dagger}(x)a_2^{\dagger}|0\rangle.\end{aligned} \tag{34}$$

Using the relation in Eq. (32), the state in the loop after scattering becomes

$$\begin{aligned}|\psi\rangle^{l}_{out} = &\frac{1}{\sqrt{2\pi}}\int d\omega e^{-i\omega t}t_1(\omega)\tilde{\phi}_{1e,in}(x,\omega)e^{-i\omega_1 t}c_e^{\dagger}(x)a_1^{\dagger}|0\rangle\\ &+\frac{1}{\sqrt{2\pi}}\int d\omega e^{-i(\omega-\omega_{12})t}t_2(\omega)\tilde{\phi}_{1e,in}(x,\omega)\\ &\times e^{-i\omega_2 t}c_e^{\dagger}(x)a_2^{\dagger}|0\rangle.\end{aligned} \tag{35}$$

By a similar analysis as previously discussed, when the scattered state in the loop traverses the coupler, it will exit completely through port a. The final output state in port a is

$$\begin{aligned}|\psi\rangle_{out} = &\frac{1}{\sqrt{2\pi}}\int d\omega e^{-i\omega t}t_1(\omega)\tilde{\phi}_{in}(x,\omega)e^{-i\omega_1 t}c_e^{\dagger}(x)a_1^{\dagger}|0\rangle\\ &+\frac{1}{\sqrt{2\pi}}\int d\omega e^{-i(\omega-\omega_{12})t}t_2(\omega)\tilde{\phi}_{in}(x,\omega)\\ &\times e^{-i\omega_2 t}c_e^{\dagger}(x)a_2^{\dagger}|0\rangle.\end{aligned} \tag{36}$$

Since we are interested in the temporal behavior of the state, we may disregard the x degree of freedom, and the state becomes

$$\begin{aligned}|\psi\rangle_{out} = &\frac{1}{\sqrt{2\pi}}\int d\omega e^{-i\omega t}t_1(\omega)\tilde{\phi}_{in}(\omega)e^{-i\omega_1 t}|\omega,1\rangle\\ &+\frac{1}{\sqrt{2\pi}}\int d\omega e^{-i(\omega-\omega_{12})t}t_2(\omega)\tilde{\phi}_{in}(\omega)\\ &\times e^{-i\omega_2 t}|\omega-\omega_{12},2\rangle.\end{aligned} \tag{37}$$

Equation (37) is the central result of this paper. We now use this result to compute the conversion efficiency for an input photonic pulse.

A. Conversion efficiency of finite-bandwidth scattering

In the following, we compute the conversion efficiency for several practically important input pulse types: Gaussian, chirped Gaussian, square, Laplace, and sech^2 pulses, all with center frequency ω_{13}, and all with the same intensity FWHM τ, as shown in Fig. 4 with axes normalized to maintain unit-area normalization (note that, in the inset, the pulses are normalized to a peak value of unity for direct visual comparison of the FWHM time duration). The inelastic frequency-shifted component of the output is given by the second term of Eq. (37):

$$\frac{1}{\sqrt{2\pi}}\int d\omega e^{-i(\omega-\omega_{12})t}t_2(\omega)\tilde{\phi}_{in}(x,\omega), \tag{38}$$

and the efficiency of frequency conversion P_c is the area ratio of the inelastic scattered component to the input pulse

$$P_c = \frac{\int d\omega|t_2(\omega)\tilde{\phi}_{in}(x,\omega)|^2}{\int d\omega|\tilde{\phi}_{in}(x,\omega)|^2}. \tag{39}$$

For monochromatic input, the Fourier component becomes a delta function in ω, so the frequency conversion approaches $|t_2(\omega)|^2$ as expected.

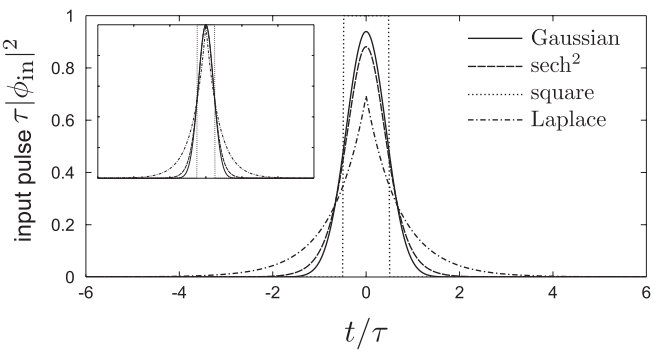

FIG. 4. Input pulse shapes with unity-area normalization. Inset shows pulses normalized to a peak value of unity, showing that all pulses have the same FWHM.

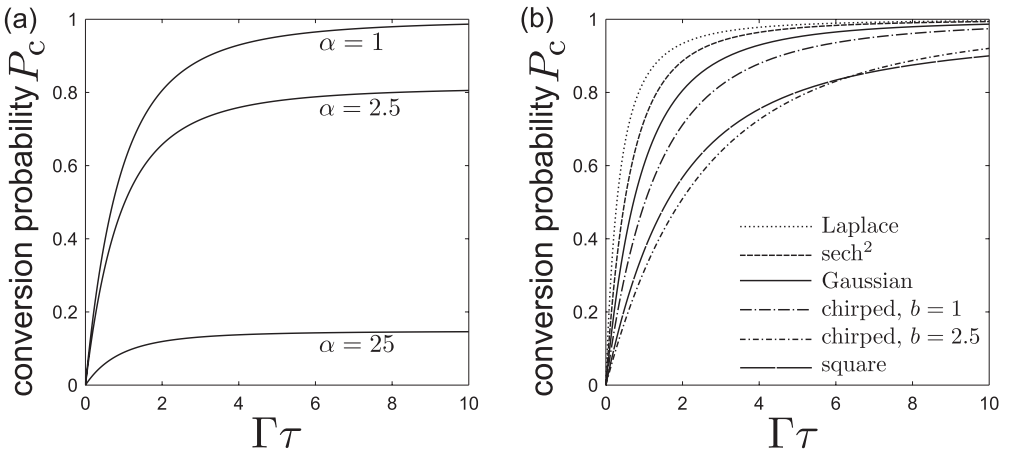

FIG. 5. Conversion efficiency for finite-bandwidth pulses in Sagnac interferometer geometry. (a) Gaussian pulse for several values of α. (b) Comparison of Gaussian, sech^2, Laplace, square, and chirped Gaussian with $\alpha = 1$.

1. Gaussian

When the input is a Gaussian pulse with intensity FWHM τ,

$$\phi_{\rm in}(x,t) = \frac{1}{\{2\pi[\tau/(2\sqrt{2\ln 2})]^2\}^{1/4}} \exp\left\{-\frac{(x-v_g t)^2}{4v_g^2[\tau/(2\sqrt{2\ln 2})]^2}\right\} e^{-i\omega_{13}(x-v_g t)/v_g}. \tag{40}$$

This and other considered pulse shapes are shown in Fig. 4. For the Gaussian input specified in Eq. (40), the Fourier component $\tilde{\phi}_{\rm in}(\omega)$ is

$$\tilde{\phi}_{\rm in}(x,\omega) = \left(\frac{2[\tau/(2\sqrt{2\ln 2})]^2}{\pi}\right)^{1/4} e^{-[\tau/(2\sqrt{2\ln 2})]^2(\omega-\omega_{13})^2} e^{i\omega x/v_g}. \tag{41}$$

When the input is normalized as in Eq. (41), the denominator of Eq. (39) will be 1. The frequency-conversion efficiency has the following analytical form:

$$\begin{aligned} P_c &= \int d\omega \left| -\frac{i2\sqrt{\Gamma_1\Gamma_2}}{(\omega-\omega_{13})+i(\Gamma_2+\Gamma_1)} \left(\frac{2[\tau/(2\sqrt{2\ln 2})]^2}{\pi}\right)^{1/4} e^{-[\tau/(2\sqrt{2\ln 2})]^2(\omega-\omega_{13})^2} e^{i\omega x/v_g} \right|^2 \\ &= \sqrt{\frac{2}{\pi}} \int d\omega \frac{4\Gamma_1\Gamma_2}{\omega^2+(\Gamma_2+\Gamma_1)^2} [\tau/(2\sqrt{2\ln 2})] e^{-2[\tau/(2\sqrt{2\ln 2})]^2\omega^2} \\ &= \frac{4\alpha}{(1+\alpha)^2} \left\{\sqrt{2\pi}[\Gamma\tau/(2\sqrt{2\ln 2})] e^{[\sqrt{2}\Gamma\tau/(2\sqrt{2\ln 2})]^2} \operatorname{erfc}[\sqrt{2}\Gamma\tau/(2\sqrt{2\ln 2})]\right\}, \end{aligned} \tag{42}$$

where $\operatorname{erfc}(z) = \frac{2}{\sqrt{\pi}} \int_z^\infty dt e^{t^2}$ is the complementary error function. The conversion efficiency is completely determined by the two dimensionless quantities $\alpha = \Gamma_1/\Gamma_2$ and $\Gamma\tau$, where $\Gamma = \Gamma_1 + \Gamma_2$. As expected, $P_c \to 4\alpha/(1+\alpha)^2 = 4\Gamma_1\Gamma_2/(\Gamma_1+\Gamma_2)^2$ as $\Gamma\tau \to \infty$. The conversion efficiency for a Gaussian pulse is shown in Fig. 5(a) for several values of α.

2. Chirped Gaussian

If the input is instead a linearly chirped Gaussian with degree of chirping determined by the dimensionless parameter b, the input is

$$\phi_{\rm in}(x,t) = \frac{1}{\{2\pi[\tau/(2\sqrt{2\ln 2})]^2\}^{1/4}} \exp\left\{-\frac{(1-ib)(x-v_g t)^2}{4v_g^2[\tau/(2\sqrt{2\ln 2})]^2}\right\} e^{-i\omega_{13}(x-v_g t)/v_g}, \tag{43}$$

so the Fourier transform is

$$\tilde{\phi}_{\rm in}(x,\omega) = \left(\frac{2[\tau/(2\sqrt{2\ln 2})]^2}{\pi(1-ib)}\right)^{1/4} e^{-[\tau/(2\sqrt{2\ln 2})]^2(\omega-\omega_{13})^2/(1-ib)} e^{i\omega x/v_g}. \tag{44}$$

The conversion efficiency is then

$$P_c = \int d\omega \left| -\frac{i2\sqrt{\Gamma_1\Gamma_2}}{(\omega-\omega_{13})+i(\Gamma_2+\Gamma_1)}\left(\frac{2[\tau/(2\sqrt{2\ln 2})]^2}{\pi(1-ib)}\right)^{1/4} e^{-[\tau/(2\sqrt{2\ln 2})]^2(\omega-\omega_{13})^2/(1-ib)} e^{i\omega x/v_g}\right|^2$$

$$= \sqrt{\frac{2}{\pi}}\int d\omega \frac{4\Gamma_1\Gamma_2}{\omega^2+(\Gamma_2+\Gamma_1)^2}\left(\frac{\tau/(2\sqrt{2\ln 2})}{\sqrt{(1+b)^2}}\right) e^{-2[\tau/(2\sqrt{2\ln 2})]^2\omega^2/(1+b^2)}$$

$$= \frac{4\alpha}{(1+\alpha)^2}\left\{\sqrt{2\pi}\frac{[\Gamma\tau/(2\sqrt{2\ln 2})]}{\sqrt{1+b^2}}\exp\left(\frac{\sqrt{2}\Gamma\tau/(2\sqrt{2\ln 2})}{\sqrt{1+b^2}}\right)^2 \mathrm{erfc}\left(\frac{\sqrt{2}\Gamma\tau/(2\sqrt{2\ln 2})}{\sqrt{1+b^2}}\right)\right\}, \tag{45}$$

so the conversion efficiency is still completely determined by α and $\Gamma\tau$ and still satisfies $P_c \to 4\alpha/(1+\alpha)^2$ as $\Gamma\tau \to \infty$ but approaches this limit more slowly than the conversion efficiency of the unchirped Gaussian.

3. Square

Now consider that the input is instead a square pulse with center frequency ω_{13} and the same intensity FWHM τ:

$$\phi_{in}(x,t) = \frac{1}{\sqrt{\tau}}\mathrm{rect}\left(\frac{x-v_g t}{v_g\tau}\right) e^{-i\omega_{13}(x-v_g t)/v_g}, \tag{46}$$

where $\mathrm{rect}(z/Z) \equiv \theta(z+Z/2)-\theta(z-Z/2)$. The Fourier transform is

$$\tilde{\phi}_{in}(x,\omega) = \frac{1}{\sqrt{\pi}}\frac{\sin[(\tau/2)(\omega-\omega_{13})]}{\sqrt{(\tau/2)}(\omega-\omega_{13})} e^{ix\omega/v_g}, \tag{47}$$

so

$$P_c = \int d\omega \left|\frac{-i2\sqrt{\Gamma_1\Gamma_2}}{(\omega-\omega_{13})+i(\Gamma_2+\Gamma_1)}\sqrt{\frac{1}{\pi}}\frac{\sin[(\tau/2)(\omega-\omega_{13})]}{\sqrt{\tau/2}(\omega-\omega_{13})} e^{-ix\omega/v_g}\right|^2 = \int d\omega \frac{4\Gamma_1\Gamma_2}{\omega^2+(\Gamma_2+\Gamma_1)^2}\frac{1}{\pi}\frac{\sin^2[(\tau/2)\omega]}{(\tau/2)\omega^2}$$

$$= \frac{4\alpha}{(1+\alpha)^2}\frac{e^{-\Gamma\tau}+\Gamma\tau-1}{\Gamma\tau}, \tag{48}$$

which is again completely determined by the dimensionless quantities α and $\Gamma\tau$ and still satisfies $P_c \to 4\alpha/(1+\alpha)^2$ as $\Gamma\tau \to \infty$ but has higher conversion efficiency than a Gaussian with equal FWHM time duration.

4. Laplace

Now consider that the input is instead a Laplacian (double exponential) pulse with center frequency ω_{13} and the same intensity FWHM τ:

$$\phi_{in}(x,t) = \sqrt{\frac{1}{\tau/\ln 2}}\exp[-|(x-v_g t)/(v_g\tau/\ln 2)|] e^{-i\omega_{13}(x-v_g t)/v_g}. \tag{49}$$

The Fourier component is a Lorentzian in ω:

$$\phi_{in}(x,t) = \sqrt{\frac{2}{\pi}}\frac{(\tau/\ln 2)^{-3/2}}{(\omega-\omega_{13})^2+(\tau/\ln 2)^{-2}} e^{ix\omega/v_g}. \tag{50}$$

The conversion efficiency is then

$$P_c = \int d\omega \left| -\frac{i2\sqrt{\Gamma_1\Gamma_2}}{(\omega-\omega_{13})+i(\Gamma_2+\Gamma_1)}\sqrt{\frac{2}{\pi}}\frac{(\tau/\ln 2)^{-3/2}}{(\omega-\omega_{13})^2+(\tau/\ln 2)^{-2}} e^{i\omega x/v_g}\right|^2 = \int d\omega \frac{4\Gamma_1\Gamma_2}{\omega^2+(\Gamma_2+\Gamma_1)^2}\left(\frac{2}{\pi}\right)\frac{(\tau/\ln 2)^{-3}}{[\omega^2+(\tau/\ln 2)^{-2}]^2}$$

$$= \frac{4\alpha}{(1+\alpha)^2}\left[\Gamma\tau\frac{\Gamma\tau+\ln 4}{(\Gamma\tau+\ln 2)^2}\right], \tag{51}$$

so the conversion efficiency is again completely determined by α and $\Gamma\tau$ and still satisfies $P_c \to 4\alpha/(1+\alpha)^2$ as $\Gamma\tau \to \infty$ but has higher conversion efficiency than a Gaussian with equal FWHM time duration.

5. Sech²

Consider finally that the input is instead a sech^2 pulse with center frequency ω_{13} and the same intensity FWHM τ:

$$\phi_{in}(x,t) = \left(\sqrt{\frac{1}{2}\frac{s}{\tau}}\right)\mathrm{sech}\left(\frac{s(x-v_g t)}{v_g\tau}\right) e^{-i\omega_{13}(x-v_g t)/v_g}, \tag{52}$$

where $s \equiv 2\text{sech}^{-1}(1/\sqrt{2})$. The Fourier transform is

$$\tilde{\phi}_{\text{in}}(x,\omega) = \sqrt{\frac{1}{2}\frac{\pi\tau}{2s}}\text{sech}\left(\frac{\pi\tau}{2s}(\omega-\omega_{13})\right)e^{ix\omega/v_g}, \tag{53}$$

so

$$P_c = \int d\omega\left| -\frac{i2\sqrt{\Gamma_1\Gamma_2}}{(\omega-\omega_{13})+i(\Gamma_2+\Gamma_1)}\sqrt{\frac{1}{2}\frac{\pi\tau}{2s}}\text{sech}\left(\frac{\pi\tau}{2s}(\omega-\omega_{13})\right)e^{ix\omega/v_g}\right|^2 = \int d\omega\frac{4\Gamma_1\Gamma_2}{\omega^2+(\Gamma_2+\Gamma_1)^2}\left(\frac{1}{2}\frac{\pi\tau}{2s}\right)\text{sech}^2\left(\frac{\pi\tau}{2s}\omega\right). \tag{54}$$

This can be written in the form

$$P_c = \frac{4\alpha}{(1+\alpha)^2}\frac{1}{2}\int d\zeta\left[\frac{1}{1+[\zeta/(a\Gamma\tau)]^2}\right]\text{sech}^2(\zeta), \tag{55}$$

where $\zeta \equiv \pi\tau\omega/[4\text{sech}^{-1}(1/\sqrt{2})]$ and $a \equiv \pi/[4\text{sech}^{-1}(1/\sqrt{2})]$, so the conversion efficiency is again a function only of the two dimensionless quantities α and $\Gamma\tau$. As $\Gamma\tau \to \infty$, the bracketed quantity in Eq. (55) approaches one for all ζ. Furthermore, one has

$$\int_{-\infty}^{\infty} d\zeta\,\text{sech}^2(\zeta) = 2, \tag{56}$$

so $P_c \to 4\alpha/(1+\alpha)^2$ as $\Gamma\tau \to \infty$. A comparison of P_c for all pulse types is presented in Fig. 5(b).

B. Effects of dissipation and dephasing

Intrinsic dissipation due to the emitter will degrade the conversion efficiency [13,14]. When the emitter dissipation rate $\gamma \equiv \gamma_c + \gamma_p$ (including both radiative decay into nonguided modes and dephasing) is included, the one-mode transmission amplitudes for the Sagnac interferometer case with $\theta = 0$ [Eqs. (23)] become

$$\begin{aligned} t_1(\omega) &= \frac{(\omega-\omega_{13})-i(\Gamma_1-\Gamma_2-\gamma)}{(\omega-\omega_{13})+i(\Gamma_1+\Gamma_2+\gamma)}, \\ t_2(\omega) &= -\frac{i2\sqrt{\Gamma_1\Gamma_2}}{(\omega-\omega_{13})+i(\Gamma_1+\Gamma_2+\gamma)}. \end{aligned} \tag{57}$$

$|t_1|^2$ and $|t_2|^2$ are plotted in Figs. 6(a) and 6(b), respectively. The on-resonance transmission with dissipation is fully determined by the dimensionless parameters α and $\bar{\gamma}$, where $\bar{\gamma} \equiv \gamma/\Gamma$ is the dissipation rate measured in units of the total transition coupling strength. In particular, $|t_1(\omega_{13})|^2 = [1-\alpha+\bar{\gamma}(1+\alpha)]^2/[(1+\alpha)^2(1+\bar{\gamma})^2]$ and $|t_2(\omega_{13})|^2 = 4\alpha/[(1+\alpha)^2(1+\bar{\gamma})^2]$. Note that $|t_1|^2+|t_2|^2$ is no longer unity due to dissipation. In fact, one has

$$|t_1|^2+|t_2|^2 = \frac{(\omega-\omega_{13})^2+(\Gamma_1+\Gamma_2+\gamma)^2-4\Gamma_1\gamma}{(\omega-\omega_{13})^2+(\Gamma_1+\Gamma_2+\gamma)^2}. \tag{58}$$

The probability of losing a photon to dissipation is given by $P_{\text{loss}} = 1-(|t_1|^2+|t_2|^2)$, which has a Lorentzian line shape and is plotted in Fig. 6(c) for several values of $\bar{\gamma}$. For fixed α and $\bar{\gamma}$, the peak of P_{loss} occurs for a photon on-resonance with the $|1\rangle \leftrightarrow |3\rangle$ transition, with the value $P_{\text{loss}}(\omega=\omega_{13}) = 4\alpha\bar{\gamma}/[(1+\alpha)(1+\bar{\gamma})^2]$. Interestingly, the peak is maximal for $\bar{\gamma} = 1$. When dissipation is further increased, the peak value is reduced. For large $\bar{\gamma}$ (i.e., a lossy emitter), P_{loss} approaches zero and $|t_1|^2$ approaches unity, indicating that the input photon does not interact with the emitter. Remarkably, the conversion efficiency P_c has an analytical result for all considered pulses except sech^2, even with dissipation. As an example, consider a Gaussian input as in Sec. III A 1. With dissipation, the conversion efficiency P_c has the analytical solution

$$\begin{aligned} P_c = \frac{4\alpha}{(1+\alpha)^2(1+\bar{\gamma})^2}\{&[\sqrt{2\pi}(1+\bar{\gamma})\Gamma\tau/(2\sqrt{2\ln 2})] \\ &\times \exp[\sqrt{2}(1+\bar{\gamma})\Gamma\tau/(2\sqrt{2\ln 2})]^2 \\ &\times \text{erfc}[\sqrt{2}(1+\bar{\gamma})\Gamma\tau/(2\sqrt{2\ln 2})]\}. \end{aligned} \tag{59}$$

With increasing $\bar{\gamma}$, the expression reaches its single-frequency limit more quickly as $\Gamma\tau$ grows, but this limit is always smaller than the nondissipative case. P_c for a Gaussian pulse with dissipation is plotted in Fig. 6(d).

Using the methods described in the appendix, we have also performed simulations which illustrate the effects of dissipation on the dynamic scattering process. Figure 7 shows input and output pulses in the frequency domain for the cases $\bar{\gamma} = 0$, $\bar{\gamma} = 0.1$, and $\bar{\gamma} = 1$ (corresponding to $\beta = 1$, $\beta = 0.91$, and $\beta = 0.5$, respectively, where the β factor gives a measure of the probability of a photon being emitted into a desired waveguide mode [16]). In all cases, the emitter is a GaAs quantum dot initialized to the $|1\rangle$ state. The frequency separation $f_{12} = \omega_{12}/(2\pi)$ is 6 GHz due to an external magnetic field of 1 Tesla [17]. For the case $\bar{\gamma} = 0$ (i.e., the dissipation is negligible), the conversion efficiency is $P_c = 0.968$. For $\bar{\gamma} = 0.1$ (i.e., $\gamma = 2\pi \times 2 \times 10^8\text{s}^{-1}$, thus $\gamma \ll \Gamma$), the conversion efficiency is $P_c = 0.804$. For $\bar{\gamma} = 1$ (i.e., $\gamma = 2\pi \times 2 \times 10^9\text{s}^{-1}$, thus $\gamma = \Gamma$), the conversion efficiency falls to $P_c = 0.248$.

C. Effects of pulse delay

In realistic experimental situations, it is challenging to meet the criteria for full quantum interference (i.e., that the two split pulses arrive at the emitter at the exact same time). We now investigate the effects of relative pulse delay as shown in Fig. 8(a). While the difference in arrival times will usually be small compared to the time duration of the pulse, this relative delay can however degrade conversion efficiency. For any given input pulse $\phi_{\text{in}}(t)$, the conversion efficiency as a function of relative delay ΔT is given by the self-convolution

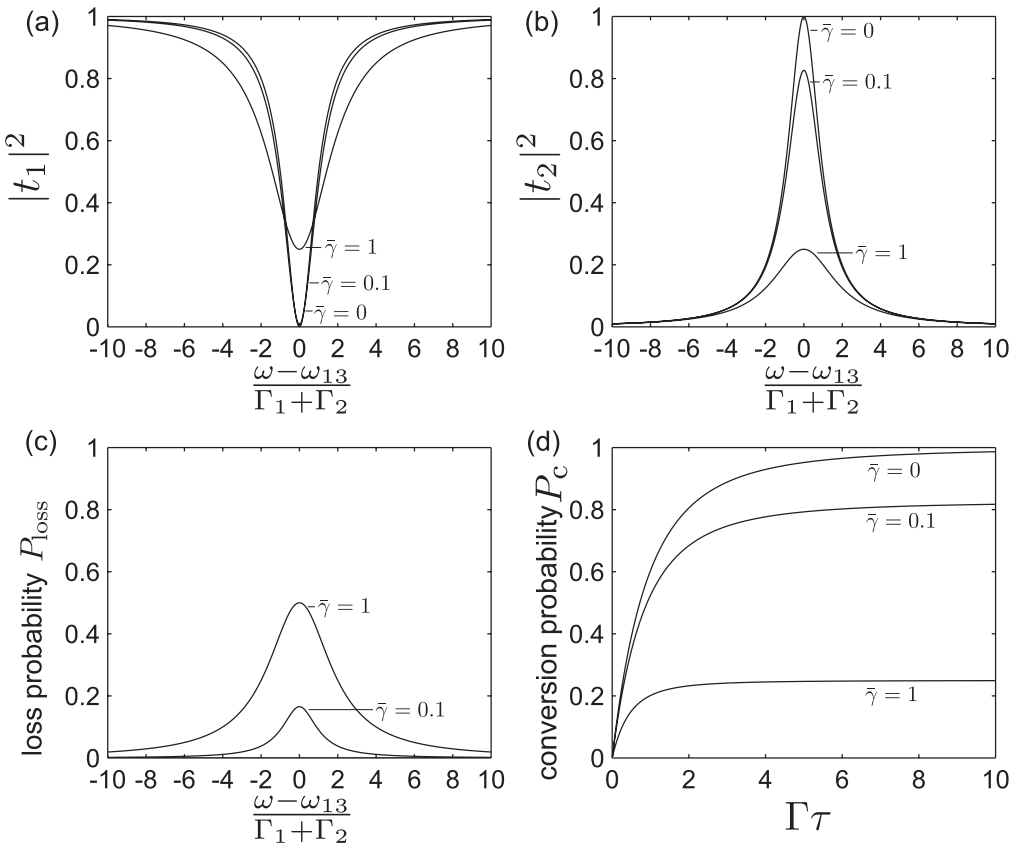

FIG. 6. Effects of dissipation. All plots correspond to Sagnac interferometer geometry with in-phase interference ($\theta = 0$). $\alpha = 1$ for all cases. (a) Frequency-unshifted transmission. (b) Frequency-shifted transmission. (c) Photon loss probability $P_{\rm loss}$. (d) Conversion efficiency for a Gaussian pulse.

of the input pulse

$$P_c(\Delta T) = P_c(0)\left(\frac{1}{2} + \frac{1}{2}\int dt|\phi_{\rm in}(t)\phi_{\rm in}(t-\Delta T)|\right), \quad (60)$$

where $P_c(0)$ is determined by α, $\bar{\gamma}$, and $\Gamma\tau$ as in Secs. III A and III B. Note that this result assumes that the cw and ccw modes are still in phase, which should always be achievable with a tunable phase shifter. The conversion efficiency as a function of ΔT is plotted for Gaussian and square pulses in Fig. 8(b) which includes both numerical and analytical [i.e., from Eq. (60)] results.

D. Optimal input pulse waveform

We have discussed above the frequency-conversion efficiency of various input pulse waveforms. In practice, the operation of the frequency-conversion process is always subject to some physical constraints. These constraints could be associated with the practical limitation of waveform generation, such as limited bandwidth, or due to practical considerations, such as a specified finite time interval T within which the quantum state transfer must occur with a prescribed probability. This optimal control problem can be formulated as a maximization problem over appropriate function spaces. The optimal control problem pertaining to the topic under discussion is to search for

$$\max \int d\omega|t_2(\omega)\tilde{\phi}_{\rm in}(\omega)|^2, \quad (61)$$

where the spectral function $\tilde{\phi}_{\rm in}(\omega)$, or its temporal representation, is subject to constraints. Such a quantum optimal control problem in general has to be solved numerically. A detailed discussion is beyond the scope of this paper (see, for example, Ref. [18]).

IV. CONCLUSION AND OUTLOOK

In this paper we have presented a theory of single photons scattering off a Λ-type three-level quantum emitter. In particular, we have shown that efficient single-photon frequency conversion can be achieved by exploiting quantum interference. The possible frequency range for implementation depends on the physical parameters of experimentally available quantum emitters. We also emphasize that the analysis is fully causal, so that pulses with different temporal forms respond differently [19]. The scheme could potentially be made more robust by placing the emitter in an optical cavity, wherein the emitter-cavity coupling strength could greatly exceed the cavity-waveguide coupling strength so as to enlarge the available bandwidth for frequency conversion. In this paper we have assumed that the emitter

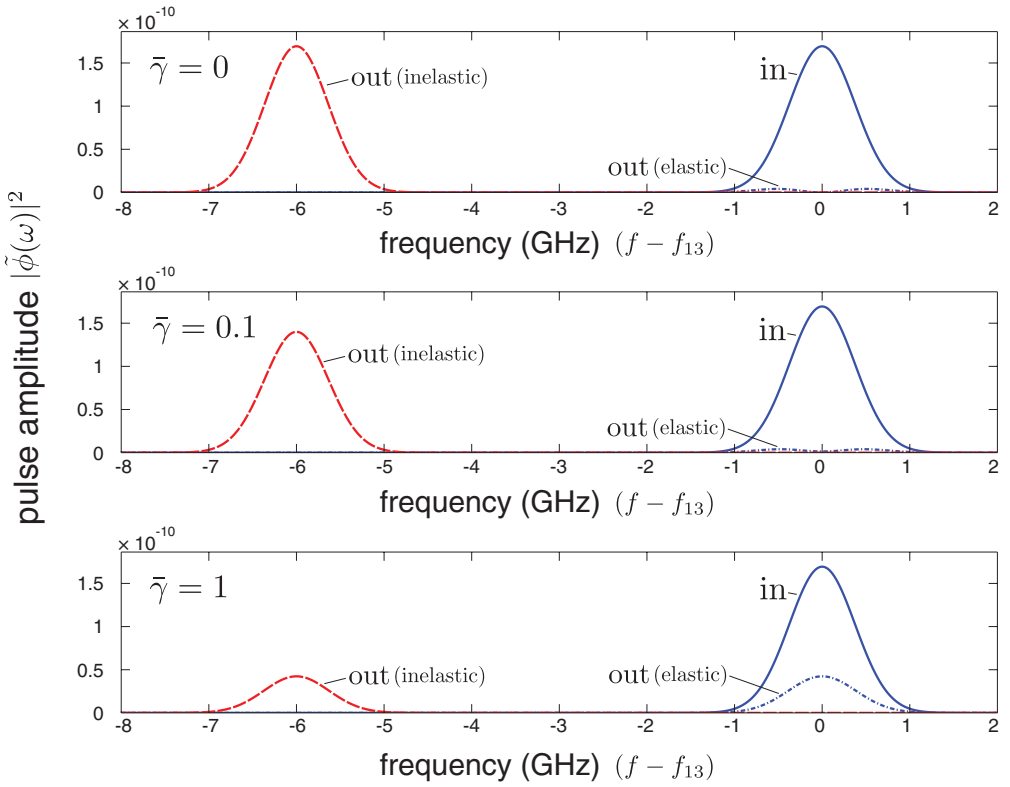

FIG. 7. (Color online) Input and output pulses in Sagnac interferometer geometry ($\theta = 0$) with dissipation. Solid blue curves are the input pulse. Dash-dotted blue curves are the elastically scattered (i.e., frequency-unshifted) outputs. Dashed red curves are the inelastically scattered (i.e., frequency-shifted) outputs. The input pulse in all cases is a Gaussian with $\tau = 0.5$ ns and center wavelength $\lambda = 819$ nm, on resonance with the $|1\rangle \leftrightarrow |3\rangle$ transition. Quantum emitter parameters correspond to the D^0-DX^0 transition in a GaAs quantum dot: coupling parameters [15] $\Gamma_1 = \Gamma_2 = 2\pi \times 10^9 \mathrm{s}^{-1}$, frequency separation $f_{12} = 6$ GHz.

couples directly to the waveguide in order to demonstrate the physics of the single-photon frequency-conversion process. Moreover, the scheme described here provides a potential mechanism to efficiently couple quantum systems operating at disparate energies, allowing hybrid quantum-information schemes [20].

Finally, we comment on some practical issues related to our scheme. First, for the single-photon frequency-conversion process to be efficient, the ability to collect a large fraction of the emitter's radiation is essential. Such a requirement also applies to a number of applications in classical and quantum information processing [21–23], as well as

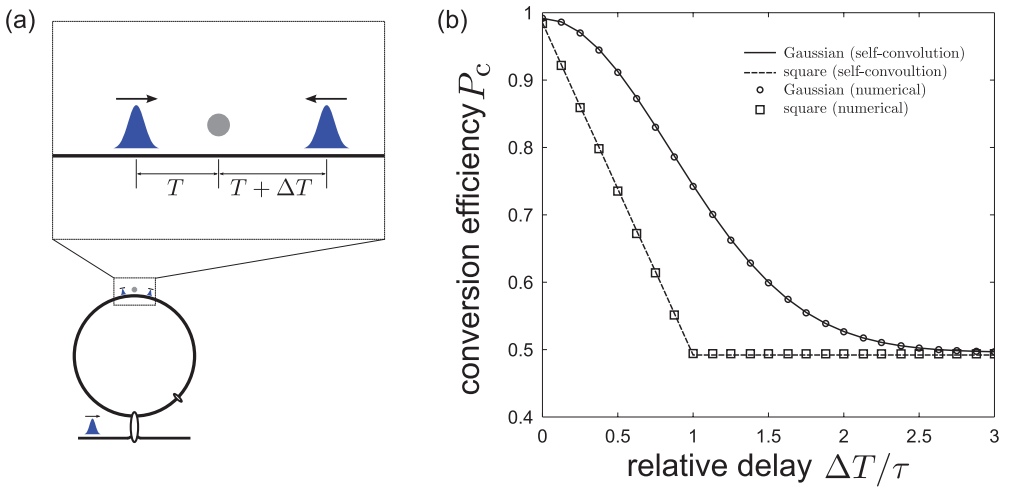

FIG. 8. (Color online) Effects of relative time delay. (a) Relative delay in arrival time between cw and ccw modes. (b) Frequency-conversion efficiency as a function of delay time.

single-emitter spectroscopy [24]. It has been shown numerically that, by embedding the emitter in a fiber-coupled semiconductor channel waveguide, the coupling efficiency can potentially be larger than 70% [25]. Moreover, the β factor has been theoretically predicted to reach as high as 0.95 in a photonic crystal waveguide [26,27]. A β factor of 0.89 has also been experimentally demonstrated [16]. In this paper, we take into account the nonideal emitter-waveguide coupling efficiency and demonstrate that the frequency-conversion efficiency is still large enough for practical applications. Second, single-photon frequency conversion has recently been reported in different geometries by using a terminated waveguide [28,29]. We emphasize that the phase coherence between each frequency component in the photonic pulse is critical for efficient single-photon frequency conversion. In this regard, our scheme is more robust in that the phase coherence is maintained, while in a terminated waveguide, the phase of the reflection amplitude is rather complicated (e.g., frequency dependent), such that the phase coherence in a terminated waveguide cannot be maintained in general. Another recent solid state proposal to achieve single-photon frequency conversion uses a periodically poled $LiNbO_3$ (PPLN) waveguide [30]. While having the advantage of not being fundamentally limited by the energy level spacing of the emitter, the scheme in Ref. [30] requires an additional strong optical field (the pump beam) and has a rather large footprint (centimeter range) due to the quasiphase-matching condition. The scheme proposed in this paper can achieve single-photon frequency conversion without being limited by these constraints, as no pump beam is required, and the Sagnac interferometer geometry is amenable to small-scale implementation, down to the μm regime [9,31,32].

APPENDIX: PSEUDOSPECTRAL METHODS AND NUMERICAL VALIDATION

To solve the dynamics of the system in a manner independent of any ansatz on the scattering states, we have also developed methods to efficiently solve the system equations of motion [Eqs. (6) and (11)] by combining highly efficient pseudospectral methods with nonuniform gridding.

1. Pseudospectral numerical scheme

To determine the full spatiotemporal dynamics of the system, we use pseudospectral [33] methods on a nonuniform grid to iteratively solve the equations of motion [Eqs. (6)]. The pseudospectral method uses the fast Fourier transform (FFT) and the fact that, in transformed space, differentiation with respect to x becomes multiplication by ik. The states are governed by equations of motion of the following form:

$$\partial_t \phi_{i\mathrm{R}}(x,t) = -v_g \partial_x \phi_{i\mathrm{R}} - iV_i \delta(x) e_3(t), \tag{A1}$$

so the evolution in time from time t_n to $t_{n+1} = t_n + \Delta t$ is given by

$$\phi_{i\mathrm{R}}(x,t_{n+1}) = e^{-v_g \Delta t \partial_x} \phi_{i\mathrm{R}}(x,t_n) - iV_i \int_{t_n}^{t_{n+1}} d\tau e^{-v_g (t_{n+1}-\tau)\partial_x} \delta(x) e_3(\tau). \tag{A2}$$

The first term on the right-hand side is evaluated in k space using the FFT, and the second term is approximated by

$$-iV_i \Delta t e^{-v_g(\Delta t/2)\partial_x} \delta(x) e_3(t_n). \tag{A3}$$

The quantity in Eq. (A3) then becomes

$$\begin{aligned} &-iV_i \Delta t e^{-v_g \Delta t \partial_x} \delta(x) e_3(t_n) \\ &= -iV_i \Delta t e_3(t_n) e^{-v_g(\Delta t/2)\partial_x} \frac{1}{2\pi} \int dk e^{ikx} \int dx e^{-ikx} \delta(x) \\ &= -iV_i \Delta t e_3(t_n) e^{-v_g(\Delta t/2)\partial_x} \frac{1}{2\pi} \int dk e^{ikx} \\ &= -iV_i \Delta t e_3(t_n) \frac{1}{2\pi} \int dk e^{-v_g(\Delta t/2)\partial_x} e^{ikx} \\ &= -iV_i \Delta t e_3(t_n) \frac{1}{2\pi} \int dk e^{-iv_g(\Delta t/2)k} e^{ikx} \\ &= -iV_i \Delta t e_3(t_n) \delta(x - v_g \Delta t/2). \end{aligned} \tag{A4}$$

For $v_g \Delta t \ll \Delta x$, the spatial shift due to time discretization is less than one spatial separation distance, so the delta function is very nearly unaffected. Consequently, the state is evolved iteratively according to

$$\phi_{i\mathrm{R}}(x,t_{n+1}) = \mathcal{F}^{-1}\left\{e^{-iv_g \Delta t k} \mathcal{F}\{\phi_{i\mathrm{R}}(x,t_n)\}\right\} - iV_1 \Delta t \delta(x) e_3(t_n), \tag{A5}$$

from a given initial state $\phi_{i\mathrm{R}}(x,0)$. Here $\mathcal{F}\{\cdot\}$ and $\mathcal{F}^{-1}\{\cdot\}$ indicate the FFT and inverse FFT respectively.

To further improve computational efficiency, we employ a nonuniform grid that has a high number of grid points around the emitter and a much coarser grid elsewhere. This allows us to take full advantage of the pseudospectral method, which (away from the scattering center) requires a grid spacing of only half the shortest wavelength of the input. We implement nonuniform gridding without introducing the need for a nonuniform discrete Fourier transform algorithm by carrying out the iteration on an auxiliary space ξ, with the transformation [34]

$$x(\xi) = \xi - \frac{a}{b} \arctan\{b(\xi\text{-}\xi_0)\}, \tag{A6}$$

which clusters grid points around $x_0 = \xi_0$ (x_0 is chosen to correspond to the emitter location). The parameter a is strictly less than 1, and gives a stronger clustering effect as it approaches 1. The parameter b determines how spread out the clustering is. After a and b are chosen to give the desired degree of clustering, ξ is defined on a uniform grid. The x grid is generated with Eq. (A6). The initial states $\phi(x,0)$ are defined on x, and iteration for $\phi(x(\xi),t)$ is carried out in ξ space. Now, using $\frac{\partial}{\partial x} \to \frac{\partial \xi}{\partial x}\frac{\partial}{\partial \xi}$, the transition function becomes

$$e^{-v_g \Delta t \partial_x} \to e^{-v_g \Delta t \partial_\xi / x'(\xi)}, \tag{A7}$$

and the iteration therefore becomes

$$\phi_{i\mathrm{R}}(x,t_{n+1}) = \mathcal{F}^{-1}\left\{e^{-iv_g \Delta t k / x'(\xi)} \mathcal{F}\{\phi_{i\mathrm{R}}(x,t_n)\}\right\} - iV_1 \Delta t \delta(x) e_3(t_n). \tag{A8}$$

Note that the grid of the transformed space variable k correspond to the ξ grid rather than the x grid. We then expand

the transition function in a series

$$e^{-iv_g\Delta tk/x'(\xi)} \approx 1 + \frac{-iv_g\Delta tk}{x'(\xi)} + \frac{(-iv_g\Delta tk)^2}{2![x'(\xi)]^2} \tag{A9}$$

and truncate higher-order terms, so the iteration takes the final form

$$\begin{aligned}\phi_{i\mathrm{R}}(x,t_{n+1}) = \phi_{i\mathrm{R}}(x,t_n) &+ \mathcal{F}^{-1}\{-iv_g\Delta tk\mathcal{F}\{\phi_{i\mathrm{R}}(x,t_n)\}\}/x'(\xi) \\ &+ \mathcal{F}^{-1}\{\tfrac{1}{2}(-iv_g\Delta tk)^2\mathcal{F}\{\phi_{i\mathrm{R}}(x,t_n)\}\}/(x'(\xi))^2 \\ &- iV_1\Delta t\delta(x)e_3(t_n).\end{aligned} \tag{A10}$$

Iterating in this manner requires more operations per iteration but can require a much smaller number of spatial grid points. In the end, the combined method results in a very efficient computational scheme.

2. Numerical confirmation of transmission spectra

Applying the computational scheme to the single-photon frequency-conversion case, we verify the transmission spectra developed in Sec. II C by specifying an input pulse ϕ_{in} and measuring the scattered pulses. The input pulse $\phi_{\mathrm{in}}(x,0)$ is specified and evolved in time. The input and output pulses as a function of time are recorded by selecting an arbitrary spatial point to the left or right of the emitter and recording the pulse at each iteration, so for example $\phi_{\mathrm{in}}(t) \equiv \phi_{1\mathrm{R}}(x_1,t)$. For the direct-incidence case, the input pulse is incoming from the left with amplitude $\phi_{1\mathrm{R,in}}(t)$, and the transmission, reflection, and excitation amplitudes are given by

$$\begin{aligned} t_1(\omega) &= \frac{\tilde{\phi}_{1\mathrm{R,out}}(\omega)}{\tilde{\phi}_{1\mathrm{R,in}}(\omega)}, \quad r_1(\omega) = \frac{\tilde{\phi}_{1\mathrm{L,out}}(\omega)}{\tilde{\phi}_{1\mathrm{R,in}}(\omega)}, \\ t_2(\omega) &= \frac{\tilde{\phi}_{2\mathrm{R,out}}(\omega-\omega_{12})}{\tilde{\phi}_{1\mathrm{R,in}}(\omega)}, \\ r_2(\omega) &= \frac{\tilde{\phi}_{2\mathrm{L,out}}(\omega-\omega_{12})}{\tilde{\phi}_{1\mathrm{R,in}}(\omega)}, \quad e_3(\omega) = \frac{\tilde{e}_3(\omega)}{\tilde{\phi}_{1\mathrm{R,in}}(\omega)}. \end{aligned} \tag{A11}$$

Here the quantities with tildes (˜) are the Fourier transforms of the numerically recorded quantities, $\tilde{\phi}(\omega) = \frac{1}{\sqrt{2\pi}}\int dt e^{i\omega t}\phi(t)$. Likewise, to validate Sagnac interferometer transmission spectra, we specify an incoming even state $\phi_{1\mathrm{e,in}}(t)$ and calculate the transmission amplitudes as

$$\begin{aligned} t_1(\omega) &= \frac{\tilde{\phi}_{1\mathrm{e,out}}(\omega)}{\tilde{\phi}_{1\mathrm{e,in}}(\omega)}, \\ t_2(\omega) &= \frac{\tilde{\phi}_{2\mathrm{e,out}}(\omega-\omega_{12})}{\tilde{\phi}_{1\mathrm{e,in}}(\omega)}, \\ e_3(\omega) &= \frac{\tilde{e}_3(\omega)}{\tilde{\phi}_{1\mathrm{e,in}}(\omega)}. \end{aligned} \tag{A12}$$

The numerically generated transmission spectra for the Sagnac interferometer case are compared to the transmission spectra through analytical methods in Figs. 3(c) and 3(d). In all cases, the resulting spectra are in excellent agreement with the analytical results.

[1] W. Stallings, *Data and Computer Communications* (Prentice-Hall, New Jersey, NJ, 2000).
[2] R. V. Roussev, C. Langrock, J. R. Kurz, and M. M. Fejer, Opt. Lett. **29**, 1518 (2004).
[3] A. P. VanDevender and P. G. Kwiat, J. Opt. Soc. Am. B **24**, 295 (2007).
[4] R. W. Boyd, *Nonlinear Optics*, 3rd ed. (Academic Press, Burlington, MA, 2008).
[5] D. E. Chang, A. S. Sorensen, E. A. Demler, and M. D. Lukin, Nat. Phys. **3**, 708 (2007).
[6] J.-T. Shen and S. Fan, Phys. Rev. A **76**, 062709 (2007).
[7] M. Bradford, K. C. Obi, and J.-T. Shen, Phys. Rev. Lett. **108**, 103902 (2012).
[8] G. Bertocchi, O. Alibart, D. B. Ostrowsky, S. Tanzilli, and P. Baldi, J. Phys. B **39**, 1011 (2006).
[9] V. M. Menon, W. Tong, C. Li, F. Xia, I. Glesk, P. R. Prucnal, and S. R. Forrest, IEEE Photonics Technol. Lett. **15**, 254 (2003).
[10] S. E. Harris and Y. Yamamoto, Phys. Rev. Lett. **81**, 3611 (1998).
[11] J.-T. Shen and S. Fan, Phys. Rev. A **79**, 023837 (2009).
[12] J. T. Shen and S. Fan, Opt. Lett. **30**, 2001 (2005).
[13] K. Srinivasan and O. Painter, Nature (London) **450**, 862 (2007).
[14] J.-T. Shen and S. Fan, Phys. Rev. A **79**, 023838 (2009).
[15] E. Finkman, M. D. Sturge, and R. Bhat, J. Lumin. **35**, 235 (1986).
[16] T. Lund-Hansen, S. Stobbe, B. Julsgaard, H. Thyrrestrup, T. Sünner, M. Kamp, A. Forchel, and P. Lodahl, Phys. Rev. Lett. **101**, 113903 (2008).
[17] C. Weisbuch and C. Hermann, Phys. Rev. B **15**, 816 (1977).
[18] A. P. Peirce, M. A. Dahleh, and H. Rabitz, Phys. Rev. A **37**, 4950 (1988).
[19] J. H. Shapiro and M. Razavi, New J. Phys. **9** (2007).
[20] M. Wallquist, K. Hammerer, P. Rabl, M. Lukin, and P. Zoller, Phys. Scr., T **137**, 014001 (2009).
[21] H. J. Kimble, Phys. Scr., T **76**, 127 (1998).
[22] S. J. van Enk, Phys. Rev. A **69**, 043813 (2004).
[23] P. Domokos, P. Horak, and H. Ritsch, Phys. Rev. A **65**, 033832 (2002).
[24] B. D. Gerardot, S. Seidl, P. A. Dalgarno, R. J. Warburton, M. Kroner, K. Karrai, A. Badolato, and P. M. Petroff, Appl. Phys. Lett. **90**, 221106 (2007).
[25] M. Davanço and K. Srinivasan, Opt. Lett. **34**, 2542 (2009).
[26] V. S. C. Manga Rao and S. Hughes, Phys. Rev. B **75**, 205437 (2007).
[27] G. Lecamp, P. Lalanne, and J. P. Hugonin, Phys. Rev. Lett. **99**, 023902 (2007).
[28] K. Koshino, Phys. Rev. A **79**, 013804 (2009).
[29] D. Witthaut and A. S. Sørensen, New J. Phys. **12**, 043052 (2010).
[30] M. T. Rakher, L. Ma, O. Slattery, X. Tang, and K. Srinivasan, Nat. Photon. **4**, 786 (2010).
[31] E. Jahn, N. Agrawal, W. Pieper, H. J. Ehrke, D. Franke, W. Furst, and C. M. Weinert, Electron. Lett. **32**, 782 (1996).
[32] V. M. Menon, W. Tong, F. Xia, C. Li, and S. R. Forrest, Opt. Lett. **29**, 513 (2004).
[33] B. Fornberg, *A Practical Guide to Pseudospectral Methods* (Cambridge University Press, Cambridge, United Kingdom, 1998).
[34] A. G. Borisov and S. V. Shabanov, J. Comput. Phys. **199**, 742 (2004).